# Fatigue crack growth under large scale yielding condition in a cast automotive aluminum alloy

Sébastien Dézécot, Matthieu Rambaudon, Alain Köster, Fabien Szmytka, Vincent Maurel, Jean-Yves Buffière

## To cite this version:

Sébastien Dézécot, Matthieu Rambaudon, Alain Köster, Fabien Szmytka, Vincent Maurel, et al.. Fatigue crack growth under large scale yielding condition in a cast automotive aluminum alloy. Materials Science and Engineering: A, 2019, 743, pp.87-97. 10.1016/j.msea.2018.03.008. hal-03962971

HAL Id: hal-03962971

https://hal.science/hal-03962971

Submitted on 30 Jan 2023

# Fatigue crack growth under large scale yielding condition in a cast automotive aluminum alloy

Sebastien Dezecot[a,b,c], Matthieu Rambaudon[b], Alain Koster[b], Fabien Szmytka[c,d], Vincent Maurel[b,*], Jean-Yves Buffiere[a]

[a] *INSA-Lyon, MATEIS, UMR CNRS 5510, 69621 Villeurbanne, France*
[b] *MINES ParisTech, PSL Research University, MAT - Centre des materiaux, CNRS UMR 7633, BP 87 91003 Evry, France*
[c] *Groupe PSA, Direction de la Recherche et de l'Innovation Automobile, Route de Gisy, 78943 Vélizy-Villacoublay, France*
[d] *ENSTA ParisTech, IMSIA, Chemin de la Hunière, 91761 Palaiseau Cedex, France*

---

## Abstract

Low cycle fatigue crack growth tests have been performed at 250 °C in order to study fatigue crack growth under large scale yielding conditions in a material widely used at high temperature by the automotive industry for cylinder head applications. The studied material was a cast aluminum alloy AlSi7Cu3Mg (close to A319) produced by Lost Foam Casting. Two different microstructures were investigated: one containing large natural pores and another where pores have been removed by Hot Isostatic Pressing (HIP). Fatigue Crack Growth Rates (FCGR) have been measured by *in situ* surface optical microscopy for different loading conditions all inducing generalized plasticity and compared to assess the influence of pores on the FCGR. *In situ* observations coupled to *post mortem* analysis revealed strong crack interactions with both pores and large hard particles on specimen surfaces and in the bulk. FCGR ranging between $10^{-6}$ and $10^{-4}$ m/cycle appear to be mainly sensitive to applied strain amplitudes. Although pores promoted secondary crack initiations and crack coalescences, they seemed to have a limited effect on steady-state FCGR which has been analytically modeled using energy densities.

*Keywords:* Low Cycle Fatigue, Cast Aluminum Alloy, Fatigue Crack Growth, Large Scale Yielding, High temperature

---

## 1. Introduction

Aluminum alloys are widely used by the automotive industry in order to reduce the weight of cars and particularly for engines parts design where the aluminum market penetration reaches 90 % [1]. Engine parts such as cylinder heads are mostly produced by foundry processes like die casting or sand casting [2]. The aluminum AlSi7Cu3Mg aluminum alloy (close to ASTM A319) which shows high values of Silicon and Copper contents is a good choice to produce cylinder heads [3, 4, 5] as it exhibits a good castability and keeps relatively high mechanical properties at elevated temperatures [6, 7]. Many car manufacturers recently tend to develop the use of alternative casting processes that allow optimizing part shapes such as the Lost Foam Casting (LFC) aiming at activating a second lever to save weight and reducing the number of machining operations after casting. LFC process however leads to coarser microstructures in terms of Secondary Dendrite Arm Spacing (SDAS) and intermetallic/eutectic particles due to its inherent slow cooling rate [8, 9]. It also tends to increase the number and size of casting defects such as shrinkage cavities and gas pores [8, 9] that mainly result from gas entrapment during sublimation of the polymeric model by the liquid metal during mold filling [10, 11]. Many studies have shown that pores and intermetallics reduce the fatigue

---

[*] Corresponding author
*Email address:* `vincent.maurel@mines-paristech.fr` (Vincent Maurel)

properties of cast aluminum [12, 13]. More precisely, hard particles (e.g. Si particles) ruptures/decohesions are observed on initiation areas and/or on crack paths for a large range of fatigue loading [14, 15, 16, 17].

Cylinder heads are subjected to severe loadings during start/stop operations that turn cylinder head inter-valve bridges into critical areas regarding Thermal-Mechanical Fatigue (TMF) [3, 18, 19]. Surface observations during Low Cycle Fatigue (LCF) and TMF tests performed on a LFC A319 alloy have shown strong crack/microstructure interactions: cracks were found to initiate at the vicinity of pores and propagated through the complex network of hard particles [9, 20]. It is however difficult to clearly understand fatigue damage mechanisms and to propose a reliable damage chronology from more 2D observations of fracture surfaces. Recent researches conducted by the authors have allowed to understand crack initiations mechanisms using *in situ* LCF testing (in large scale yielding conditions) at 250 °C on miniature specimens monitored by X-ray synchrotron tomography [21]. It was found that crack initiation takes place in the specimen bulk and are caused by the rupture of hard particles located near large shrinkage pores which induce high inelastic strain localization and high stress triaxiality levels in their vicinities [22]. The resulting short cracks tend then to propagate along the hard particles network. It was also shown that a criterion based on the local dissipated inelastic energy densities allows to correctly predict crack initiation areas at the scale of the microstructure [22]. However, because of the small specimens dimensions, it was not possible to investigate the influence of the *pore network* on crack propagation.

LCF tests are generally used to study fatigue lifetimes (number of cycles to failure) of structural materials such as aluminum alloys under severe loading conditions in order to identify fatigue lifetime criteria that can be used by designers [20, 23, 15, 24]. Fatigue crack growth within cast aluminum alloys under large scale yielding conditions and at high temperature is however barely studied: analyses are usually restricted to specific domains where aluminum alloys are not used for critical parts. This kind of tests may however be an attractive tool to study engine inter-valve bridges rupture. Few fatigue crack growth models are therefore available for LCF tests at high temperatures [25, 26, 27]. Fatigue crack growth modeling is classically based on elastic loading and/or on the J integral concept. However, this kind of approach is not valid for cases where plasticity cannot be neglected. Shih and Hutchinson proposed to decompose J in an elastic and a plastic part as $J = J_e + J_p$ [28]. They first approximated the plastic behavior assuming non-linear elasticity and then extended it to fully elastic-plastic behavior using a Ramberg-Osgood law. However, this kind of approach cannot be used with more complex mechanical behaviors such as viscoplasticity. Recently, fatigue crack propagation rate in elastic-plastic materials has been successfully modeled using the J-integral concept but it requires complex tools such as configurational mechanics [29]. Based on the idea of energy partitioning, Maurel et al. also proposed a model based on the energy decomposition into an elastic and a dissipated inelastic part that allowed to correctly model fatigue crack growth for a ferritic stainless steel [30], a nickel-based and a cobalt-based superalloys [31, 32] for a large range of applied strain levels. As it was done in these studies, Single Edge Notch Tension (SENT) specimens are a straightforward test that can be used to observe fatigue crack growth and to identify the model parameters under large scale yielding condition.

In this paper we first describe the fatigue crack growth mechanisms observed *in situ* on SENT fatigue specimen tested under large scale yielding conditions at 250 °C on a LFC AlSi7Cu3Mg alloy. The influences of pores and hard particles networks on the crack paths are identified by comparison with a pore-free material. Fatigue Crack Growth Rates (FCGR) are measured for both materials. In a second part, an analytical model based on an energetic approach is proposed and used to model FCGR.

## 2. Materials

A cast aluminum AlSi7Cu3Mg (close to A319) alloy has been tested in this study. Its chemistry was analyzed by spark optical emission spectrometry and is reported in Table 1. This material is used to produce cylinder heads by the Lost Foam Casting (LFC) process. The process parameters (mainly cooling rates) have been here adapted in order to obtain a coarser microstructure which allows to easily observe damage mechanisms and to understand the role played by microstructure and pores [22]. This reference material was overaged during 500 h at 250 °C after solidification in order to obtain stabilized microstructures and the targeted mechanical properties [33]. Its resulting microstructure is typical of hypo-eutectic cast aluminum alloys with a dendritic structure [22].

Although these alloys are mainly characterized (for static mechanical properties) by their SDAS - here 76.1 ± 9.4 µm - numerous other microstructural features are known to have an impact on their fatigue behaviors: this is especially the case of secondary hard phases and pores [34, 35, 14, 20]. Since no solutionizing was carried out during the material thermal history, eutectic silicon particles are interconnected and keep acicular shapes [36]. The size of those Si particles is relatively large: forty percents of the Si particles have a Feret diameter above 20 µm and, despite an exponential decrease, some exceed 100 µm. Fe- and Cu-rich phases have even more complex 3D shapes [21] and their Feret diameters can reach several hundred micrometers. Pores are however known to have the more detrimental effect on the cyclic properties of cast alloys. In addition to SDAS, the porosity or the pore size distribution are therefore the common microstructural parameters used to estimate/model fatigue lifetimes. The studied material presents a porosity of 1.07 %. It was estimated on a volume of 360 mm$^3$ acquired by Computed Tomography (CT) with a 7 µm voxel size. Figure 1 allows a more exhaustive description of the pores population. It reveals on subfigure 1a that the pore equivalent spherical diameter $\varnothing_{eq}^{spherical}$ reaches up to 650 µm and that pores with an equivalent diameter below (or equal to) 100 µm represent 98.65 % of pores in number. However, the 1.35 % remaining and largest pores (over 100 µm, mainly shrinkage cavities) generate approximatively 91 % of the total porosity as visible on figure 1b which shows the cumulative porosity fraction curve.

| Elements | Si | Fe | Cu | Mn | Mg | Ni | Zn | Ti | Cr |
|---|---|---|---|---|---|---|---|---|---|
| Wt % | 7.30 | 0.10 | 3.45 | < 0.004 | 0.31 | 0.048 | < 0.02 | 0.10 | < 0.012 |

Table 1: Chemical composition of the studied alloy.

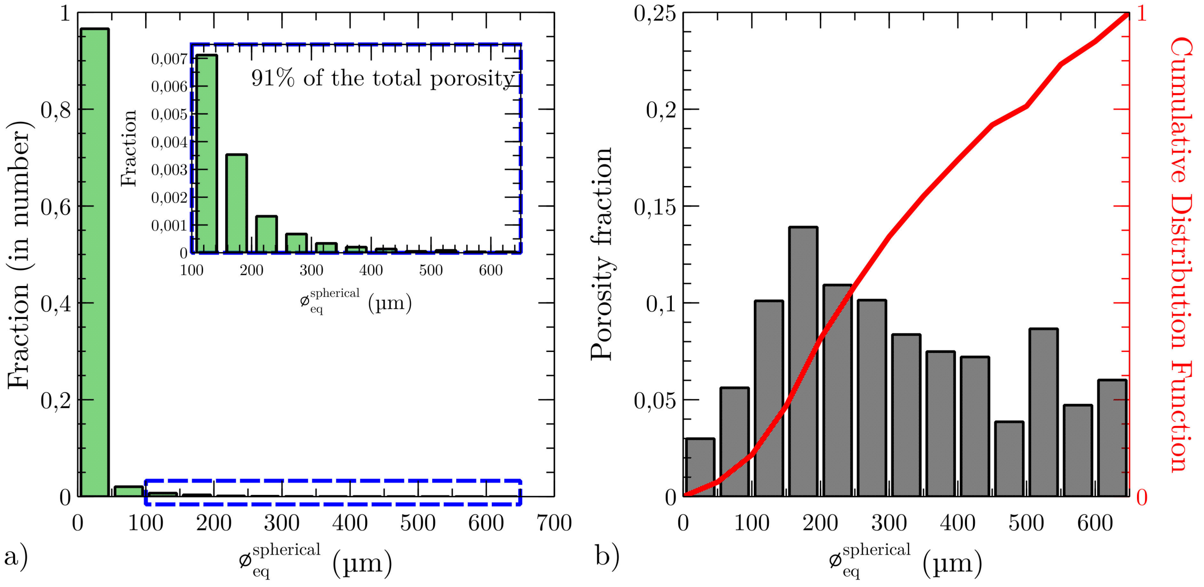

Figure 1: (a) Histogram of pore equivalent spherical diameters $\varnothing_{eq}^{spherical}$ the insert shows a zoom on the tail of the curve (pores larger than 100 $\mu$m). (b) Distribution of the porosity fraction as a function of $\varnothing_{eq}^{spherical}$; the right axis shows the cumulative distribution function of the porosity fraction.

A second material was developed for this study to determine the role of hard phases and pores on the fatigue behavior of materials produced by LFC. A Hot Isostatic Pressing (HIP) treatment was performed on bars of the previously described LFC overaged material in order to remove pores before machining [37]. During this treatment, a pressure of 1000 ± 30 bars is applied at 485 ± 10 °C during 2 h under Argon atmosphere. Both cooling and depressurization steps were then carried out naturally. Temperatures reached during the HIP treatment are too low to cause an alteration of the eutectic hard particles (e.g. Si particle spheroidization). No change of their sizes and shapes were indeed observed [38]. As reported in table 2, a hardening, probably due to a partial solutionizing of nanometric $\theta$-$Al_2Cu$ precipitates is observed after HIP treatment. It is then necessary to transform resulting $\theta'$ (or $\theta''$) into $\theta$ by an appropriate over-aging heat treatment to proceed to robust comparisons. An additional aging heat treatment which consists of 60 hours at 250 °C was therefore applied to the HIP-ed material to obtain mechanical properties (hardness in intra dendritic regions) similar to those of the non HIP-ed material.

| | Macro Hardness HV (10 kg) | | Micro Hardness HV (50 g) | |
|---|---|---|---|---|
| | Average | Standard deviation | Average | Standard deviation |
| LFC | **57** | 5.1 | **45** | 1.9 |
| LFC + HIP | 83 | 5.4 | 71 | 4.6 |
| LFC + HIP + 60 h at 250°C | **56** | 2.0 | **44** | 1.8 |

Table 2: Macro- and micro- Vickers hardness for three material configurations. Micro-Hardness tests were performed directly in the dendritic phase in order to be able to observe modifications of the aluminum matrix precipitation state.

## 3. Experimental protocols and measurements

### *3.1. Specimen preparation*

Fatigue crack growth specimens used for this study are of SENT type. All dimensions are reported on figure 2. Specimens have been machined by electro-discharge machining (including notches) from cylindrical bars which have been directly extracted from cylinder head inter-valves bridges [38]. Sample surfaces were prepared by mechanical polishing down to a 1 µm diamond solution to avoid crack initiation on surface scratches. The root of the notch is left unpolished because of its small radius of curvature (100 µm). Specimens were finally separated into two categories referenced as **P** and **PF** for respectively Porous and Pore-Free materials. Specimens are not pre-cracked as the presence of the notch produces a strain localization large enough to control the first crack initiation area.

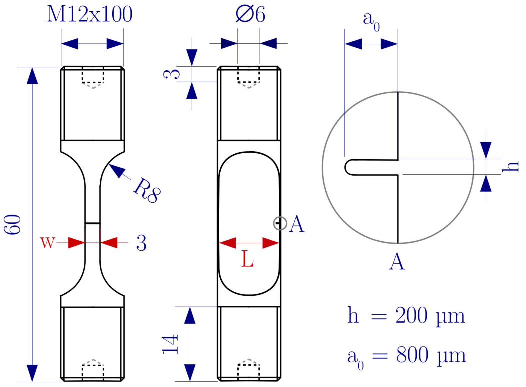

Figure 2: Geometry of SENT specimen used for the LCF tests (if not precised dimensions are in mm.

### *3.2. Pre- and Post-mortem characterization*

All samples were characterized by laboratory X-ray Computed Tomography (CT) before and after tests in order to control their microstructures (mainly pores for the **P** material) and to analyze the crack path after cycling. A GE Phoenix V|tome|X 3D X-ray tomograph equipped with an X-ray microfocus source has been used with an acceleration voltage of 80 kV and an intensity of 180 µA. Scans were performed with a 7 µm voxel size. Because of the polychromatic cone beam, Si particles are not visible on tomographic reconstructions. The specimen gauge lengths have been entirely imaged. Figure 3 shows a 3D rendering of the pores and the external surfaces of two specimens from **P** batch. *Post mortem* surface observations have been carried out on the two faces of each specimen ((x,y) planes on figure 3) by optical microscopy in order to analyze cracks interactions with microstructural features which are identified by a morphological analysis. Particles are then compared to literature studies [9, 39, 40] and a reference EDX analysis[38] in order to validate the choices previously made.

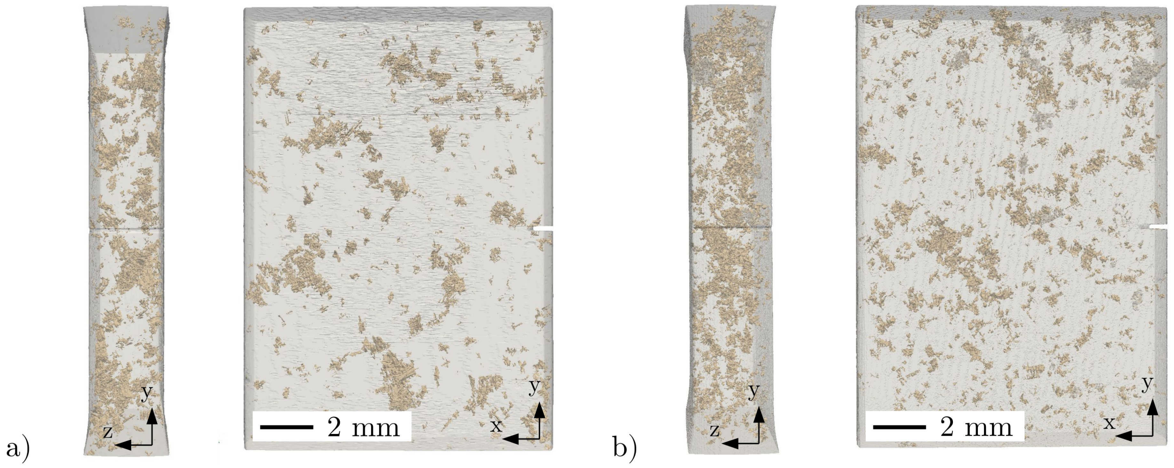

Figure 3: 3D renderings of the pores within the gauge length of specimen P3 [$\Delta\varepsilon/2 = 0.125\%$ | $R_\varepsilon = 0$] (a) and P1 [$\Delta\varepsilon/2 = 0.0625\%$ | $R_\varepsilon = 0$] (b) before testing.

### *3.3. Low cycle fatigue crack growth tests*

Isothermal LCF crack growth tests have been carried out on SENT specimens at a constant frequency of 0.1 Hz using an electro-mechanical INSTRON 8561 machine. A lamp furnace was used to heat the specimens at 250 °C in the gauge zone and the thermal regulation was performed via a type K thermocouple directly fixed on one of the notch side. The tests were controlled by longitudinal total strain measured on a 10 mm reference length using a high temperature extensometer fixed on the sample edge opposite to the notch. A triangular shape signal was used for strain control. Table 3 reports the loading conditions for each studied specimen. Their strain/stress curves after two cycles are reported on figure 4 exhibiting large scale yielding condition (except for P1). Tests were conducted in air environment.

| Specimen | Material | $R_\varepsilon$ | $\varepsilon_{max}$ (%) | $\Delta\varepsilon/2$ (%) | $\dot{\varepsilon}$ ($s^{-1}$) |
|---|---|---|---|---|---|
| P1 | LFC | 0 | 0.125 | 0.0625 | $2.5 \times 10^{-4}$ |
| P2 | LFC | -1 | 0.125 | 0.125 | $5.0 \times 10^{-4}$ |
| P3 | LFC | 0 | 0.250 | 0.125 | $5.0 \times 10^{-4}$ |
| P4 | LFC | -1 | 0.250 | 0.250 | $1.0 \times 10^{-3}$ |
| PF1 | LFC+HIP+Aging | -1 | 0.125 | 0.125 | $5.0 \times 10^{-4}$ |
| PF2 | LFC+HIP+Aging | 0 | 0.250 | 0.125 | $5.0 \times 10^{-4}$ |
| PF3 | LFC+HIP+Aging | 0 | 0.350 | 0.175 | $7.5 \times 10^{-4}$ |

Table 3: Loading conditions applied to SENT specimens at 250 °C.

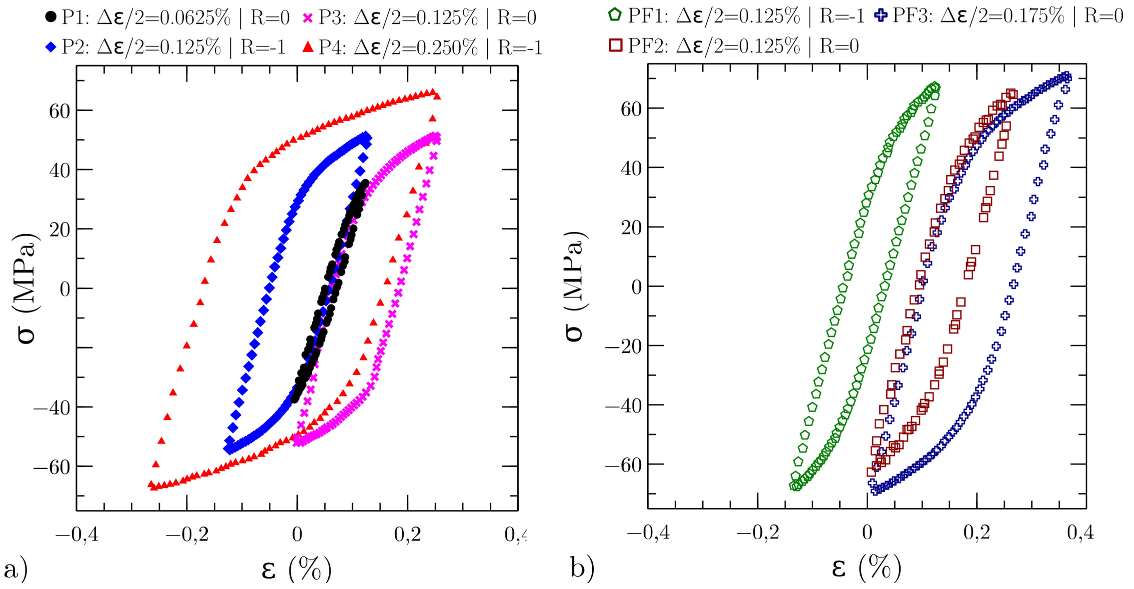

Figure 4: Strain/Stress loops at N=2 for the (a) porous material -**P**- and (b) the pore-free material -**PF**-.

### *3.4. Crack growth monitoring*

A video of one side of the specimen was acquired during the tests in order to follow the crack propagation. Pictures were taken at each maximum and minimum load, through a hole machined in the furnace, using a numerical microscope Keyence VHF-700F equipped with a Z00 optic which is compatible with high focal distance (around 8.5 mm here). The camera was fixed on a rigid structure to the machine frame and consistently records pictures on the same area (a surface of 7.2 mm × 5.4 mm) in order to easily detect the crack growth. The magnification was limited due to the large analyzed area and the pixel size was fixed at 5 µm. In accordance to the Nyquist sampling criteria the spatial resolution was equal to 11.5 µm [41].

### *3.5. Crack length measurement*

Crack length measurement is of primary importance when dealing with fatigue lifetime modeling. Although crack length $a$ is commonly estimated by the length of the crack projection $a_{proj}$ on the plane orthogonal to the loading direction during uni-axial fatigue tests, a curvilinear crack length $a_{curv}$ better represents the real crack length when large and numerous crack deviations are observed (see figures 6 and 7). For specimen P2, $a_{curv}$ is 27 % longer than $a_{proj}$ at the end of the test for instance. $a_{curv}$ is thus chosen to represent the crack length in this study.

FCGR have been calculated using the relation $da/dN = \Delta a_{curv}/\Delta N$ with a prescribed incremental $\Delta a_{curv}$. $\Delta N$ values have been identified for each iteration from the crack propagation movies. Figure 5 exhibits three different crack measurement protocols for a specimen containing pores (P2) and for a HIP-ed specimen (PF2). The first technique, called $\Delta N$ ***best shape***, consists in dividing crack into as many segments as necessary in order to preserve its shape, while others consist in dividing cracks at fixed crack length increments $\Delta a$. Coalescence phases are systematically excluded from the measurements in order to only obtain the FCGR of the main cracks. Crack coalescences are visible on curves representing the crack lengths as a function of the number of cycles by crack length jumps. In accordance with subfigures 5b and 5d the spatial increment was here fixed to 200 µm in order to be less sensitive to cracks interactions with microstructural features such as Si particles, intermetallic phases, and pores which lead to important and sudden FCGR fluctuations. This relatively large increment of crack length acts as a filter and allows to extract the steady-state FCGR on experimental performed tests [38].

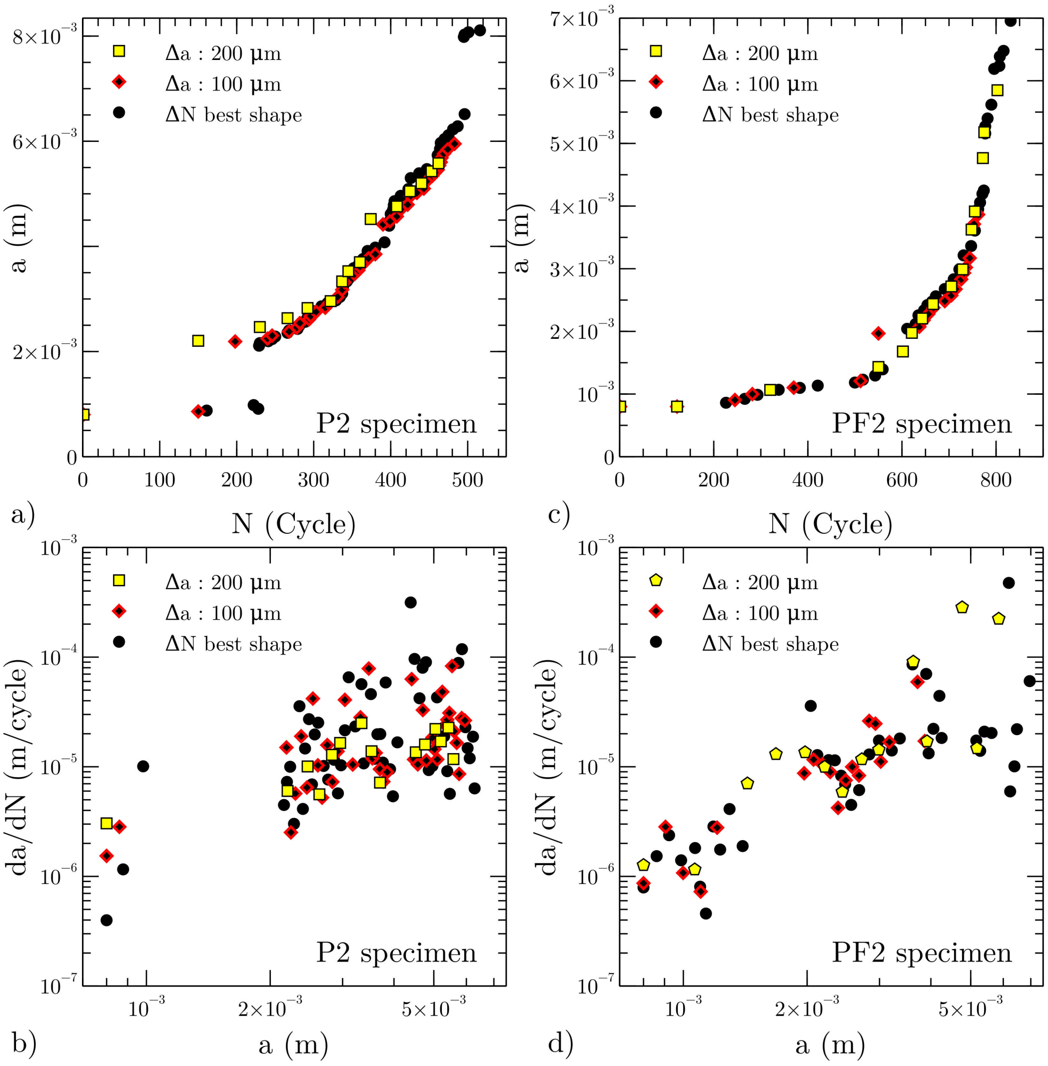

Figure 5: Comparison of different measurement protocols for crack lengths and for crack growth rates estimations. Sub-figures (a) and (c) respectively show the evolution crack length as a function of the number of cycles for a **P** (P2 specimen, $[\Delta\varepsilon/2 = 0.125\% \mid R_\varepsilon = -1]$) and a **PF** (PF2 specimen, $[\Delta\varepsilon/2 = 0.125\% \mid R_\varepsilon = 0]$) specimen. Sub-figures (b) and (d) correspond to the evolution of the crack growth rates as a function of the crack length for both previous specimens.

### *3.6. Fatigue crack growth rates modeling*

A model describing steady-state FCGR is proposed to account for the experimental data: it relies on the proposition of Maurel et al. and is based on an energetic approach [30]. The energy was decomposed into an opening elastic part $W_e$ and a dissipated inelastic energy $W_p$. In the general case, those two terms can be written as:

$$W_e = \frac{1}{3}\int_{cycle} < tr(\underline{\underline{\sigma}}) >< tr(d\underline{\underline{\varepsilon}}_e) > \tag{1}$$

$$W_p = \int_{cycle} \underline{\underline{s}} : d\underline{\underline{\varepsilon}}_p \tag{2}$$

where $\underline{\underline{s}}$ is the deviatoric part of the stress tensor, $tr()$ is the first invariant and $<>$ is the Macaulay bracket ($< \cdot >= \cdot$ if $\cdot > 0$ and $< \cdot >= 0$ if $\cdot <= 0$).

In the case of uni-axial tests and a macroscopic approach, these energies are similar to those previously proposed by Xia and Ellyin [42, 43] and can be estimated from the experimental data by the following equations:

$$W_e = \frac{1}{3}(1-2\nu) \int\limits_{cycle} \sigma \cdot d\varepsilon_e \tag{3}$$

$$W_p = \int\limits_{cycle} \sigma \cdot d\varepsilon_p \tag{4}$$

$\sigma$, $\varepsilon_e$ and $\varepsilon_p$ are respectively the nominal stress ($\sigma = \sigma_{yy}$), the elastic and plastic longitudinal strain ($\varepsilon = \varepsilon_{yy}$, measured by the extensometer).

FCGR are given by the following relationship which is a sum of two power law functions:

$$\frac{da}{dN} = \lambda \left[ \left( \frac{W_e}{\gamma_e} a \right)^{m_e} + \left( \frac{W_p}{\gamma_p} a \right)^{m_p} \right] \tag{5}$$

$\lambda$ is a material characteristic length, $\gamma_e$ and $\gamma_p$ are two material dependent surface energies and, $m_e$ and $m_p$ are two material exponents. $m_e$ is considered as equal to half the Paris exponent and the value of the $m_p$ parameter should be close to 1 [30].

In order to take into account the surface reduction, associated with the crack growth, in the nominal stress estimation, the remaining material ligament has been evaluated for each cycle. A linear crack front has been assumed through the sample thickness to estimate the effective surfaces by the relationship $S(N) = w \cdot (L - a_{proj}(N))$ (L and $w$ are detailed on figure 2).

The value of $\lambda$ was chosen equal to the SDAS value (76.6 µm) and the elastic exponent $m_e$ was evaluated at 2.8 from the work of Mehry et al. [15]. The plastic exponent $m_p$, which corresponds to the slope of the FCGR curve of a fully plastic test (where $W_e$ can be neglected), was estimated at 1.6. Other model parameters ($\gamma_e$, $\gamma_p$) have been identified using an iterative optimization process based on a residual minimization by least square method [30] for each material.

## 4. Results

### 4.1. Fatigue crack growth mechanisms

This section describes the LCF crack growth and highlights cracks interactions with the local microstructure in order to identify fatigue mechanisms. Pictures obtained from the *in situ* surface crack monitoring are analyzed first for two specimens of representative behavior detailed in figure 5.

Figure 6 shows the crack evolution at numerous number of cycles in specimen P2. On all subfigures, yellow arrows without labels highlight cracks fronts (including fronts of secondary cracks). As visible on the subfigure 6a, it is necessary to apply 152 loading cycles on the P2 specimen to observe the main crack initiation from the notch tip (label a1). From that point, a complex crack path is observed (until N=546 cycles, see figure 6f) which is typical of strong crack/microstructure interactions. The first main interactions occur in areas identified by label b1 and c1. After the main crack initiation, a second micro-crack labeled b1 initiates on a shrinkage cavity located around 600 µm in front of the notch (subfigure 6b). The subfigure 6c shows the coalescence of the main crack (marker c1) with this new one at N=300 cycles. It is important to notice that this second crack also grows between cycles N=214 and N=300. It is likely that this crack coalescence occurs earlier in the bulk of the specimen. A large crack deviation (marker d1) observed on subfigure 6d and 6e is also the result of strong interactions with microstructure. The local bright area at N=400 cycles corresponds to an abnormal light reflexion due to a large specimen surface disorientation which is the consequence of the high level of inelastic strain localization. The crack goes directly through this area. Secondary cracks initiate on the left part of subfigure 6e. One of them appears in the aluminum matrix (label e1) and another one in the vicinity of a shrinkage cavity located in the top left corner (label e2). The main

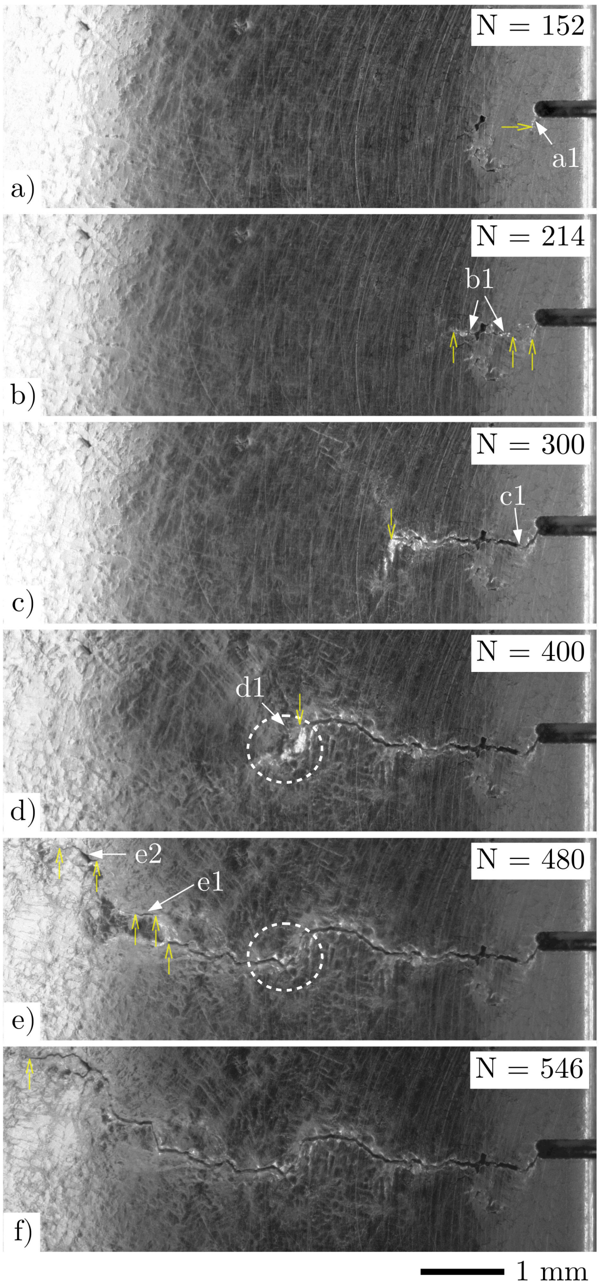

Figure 6: Optical micrographs recorded *in situ* at the maximum load that illustrate crack propagation in the material containing pores (P2 specimen). All markers labeled from a1 to e2 (white plain arrows) point on main events. Other arrows (in yellow) highlight successive cracks fronts positions. ($\Delta\varepsilon/2 = 0.125\%$ and $R_\varepsilon = -1$)

crack then deflects to coalesce with those secondary cracks, underlining again the microstructure/cracks interactions.

Figure 7 shows a similar crack path for the pore-free material submitted to different loading conditions, specimen PF2. Crack initiation here occurs after several hundred of cycles (363 cycles), see label a1' on subfigure 7a. Although this specimen is free of pore, the final crack path also appears to be strongly tortuous when a lot of secondary cracks initiates at markers b1', c2' and, e1'. The main crack coalesces with these secondary cracks in areas presenting the highest crack deviations. The angle by which the crack is deflected relative to the plane orthogonal to the loading direction can reach up to around 90° as shown by marker c1' (subfigure 7c). The "sawtooth" path visible after the $786^{th}$ cycle (labels d1' and e1') corresponds to successive micro-crack initiation/crack coalescence phenomena. The crack has a complex shape that is formed by rupture/debonding of hard particles. Once microcracks are formed in the vicinity of hard particles, the main crack can be deflected (coalescence) and causes an irregular crack shape.

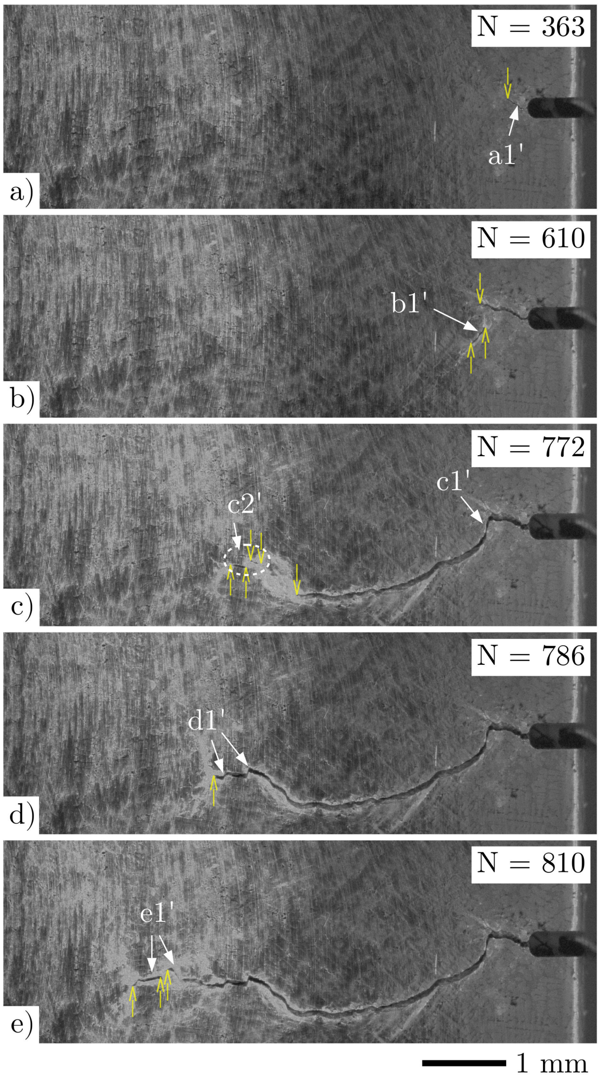

Figure 7: Optical micrographs recorded *in situ* at maximum load that illustrate crack propagation in the pore-free material (PF2 specimen). All markers labeled from a1' to e1' (white arrows) point on main events. Other arrows (in yellow) highlight successive positions of the cracks fronts. ($\Delta\varepsilon/2 = 0.125\%$ and $R_\varepsilon = 0$)

*Post mortem* optical analysis of crack paths allow to perform complementary observations to determine more precisely the role of the microstructural features on the crack behavior. Figure 8a reveals the crack path on the P2 specimen surface which was not monitored *in situ*. Comparison with figure 6 shows that the crack does not have the same morphology on each face of the sample. Many crack/pores and crack/hard particles interactions are highlighted on subfigures 8b and 8c. These enlarged images correspond to areas shown in red on subfigure 8a. They reveal that the crack is mainly driven through the local microstructure by rupture/decohesion of hard particles (Si particles, $Al_2Cu$, Fe-rich intermetallics) located in front of the crack tip. Crack branching is also observed on subfigure 8b. These fragmentations of particles are, in addition of pores for **P** specimens, also a source of secondary crack initiation that lead to crack coalescences, especially on the **PF** material.

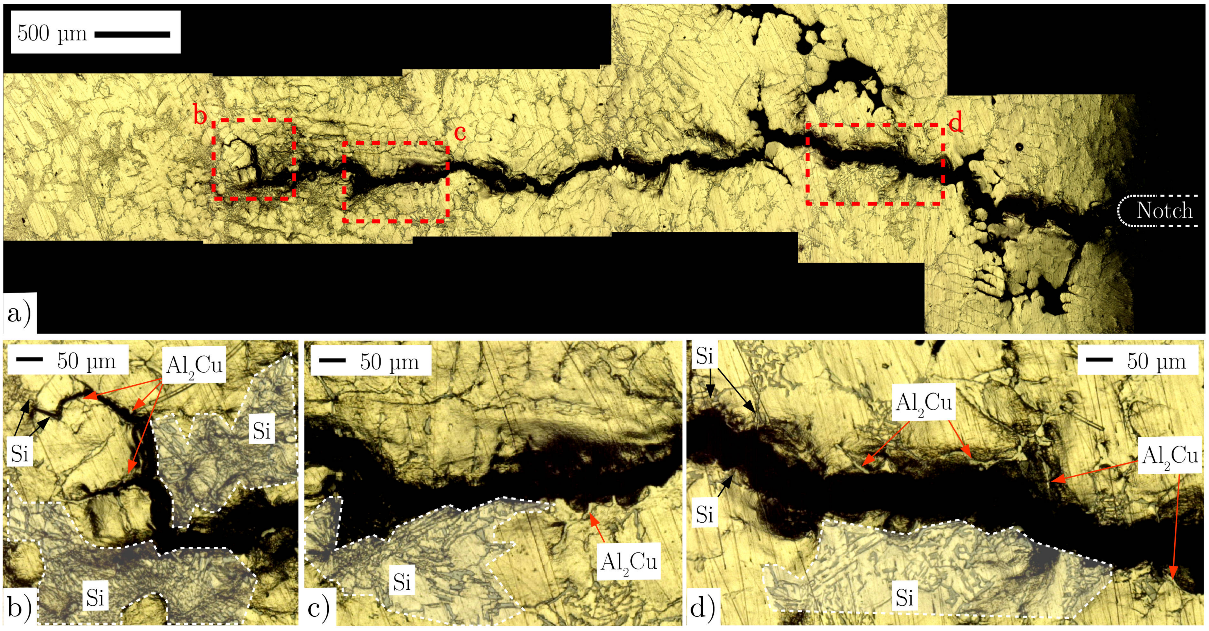

Figure 8: *Post mortem* optical micrographs (a) of specimen P2 containing pores (opposite side of the face observed figure 6). Subfigures (b), (c) and (d) are magnifications of areas shown in red on subfigure (a).

*Post mortem* CT analysis gives supplementary details about crack behavior through the whole volume of the specimen. Figure 9 shows numerous tomographic slices in the plane orthogonal to the main crack growth direction (X axis of subfigure 9a) located at a distance L from the notch root. Si particles are not visible on these tomographic slices due to the close X-ray attenuation coefficients between aluminum and silicon but one can assume they also play a major role. Pores intersecting the crack are highlighted in boxes in red. Using the 3D information, one can infer that pores strongly affect the crack path as the crack progressively joins the pores located close to its front. Crack height variations larger than 1 mm (along y axis) are consecutively observed. When no pore is located close to the crack front, large $Al_2Cu$ phases cause crack deviations like in the cases of specimen P2 (see yellow ellipses on figure 9).

### *4.2. Fatigue crack growth rates*

Figure 10 shows experimental FCGR evolutions on the basis of FCGR obtained for a $\Delta a = 200\,\mu\mathrm{m}$ as described in section 3.5 and considering only FCGR in a "steady-state" approximation where sudden accelerations due to pores are ignored. Subfigures 10a and 10b respectively give results for **P** and **PF** materials. The first noticeable result is that larger applied strain amplitudes, result in larger FCGR. For instance, subfigure 10a shows FCGR in the range of $10^{-8}$ to $10^{-6}$ m/cycle in the case of limited plastic strain (see P1 curve on figure 4). However FCGR range between $10^{-6}$ m/cycle and $10^{-4}$ m/cycle for loading conditions corresponding to extended plasticity. No major differences are observed between the two materials: pores seems to have a limited effect on FCGR when using the "steady state" FCGR measurement for specimens tested under large scale yielding condition (especially at $\Delta\varepsilon/2 = 0.125\%$). It also appears that for a given strain amplitude, FCGR does not depend on the R ratio value as shown for specimens P2/P3 and PF1/PF2: this reinforces the idea of using an energy densities based model. Stress/strain loops of P2/P3 and PF2/PF3 specimens also appear similar on figure 4 reinforcing the assumption that pores only

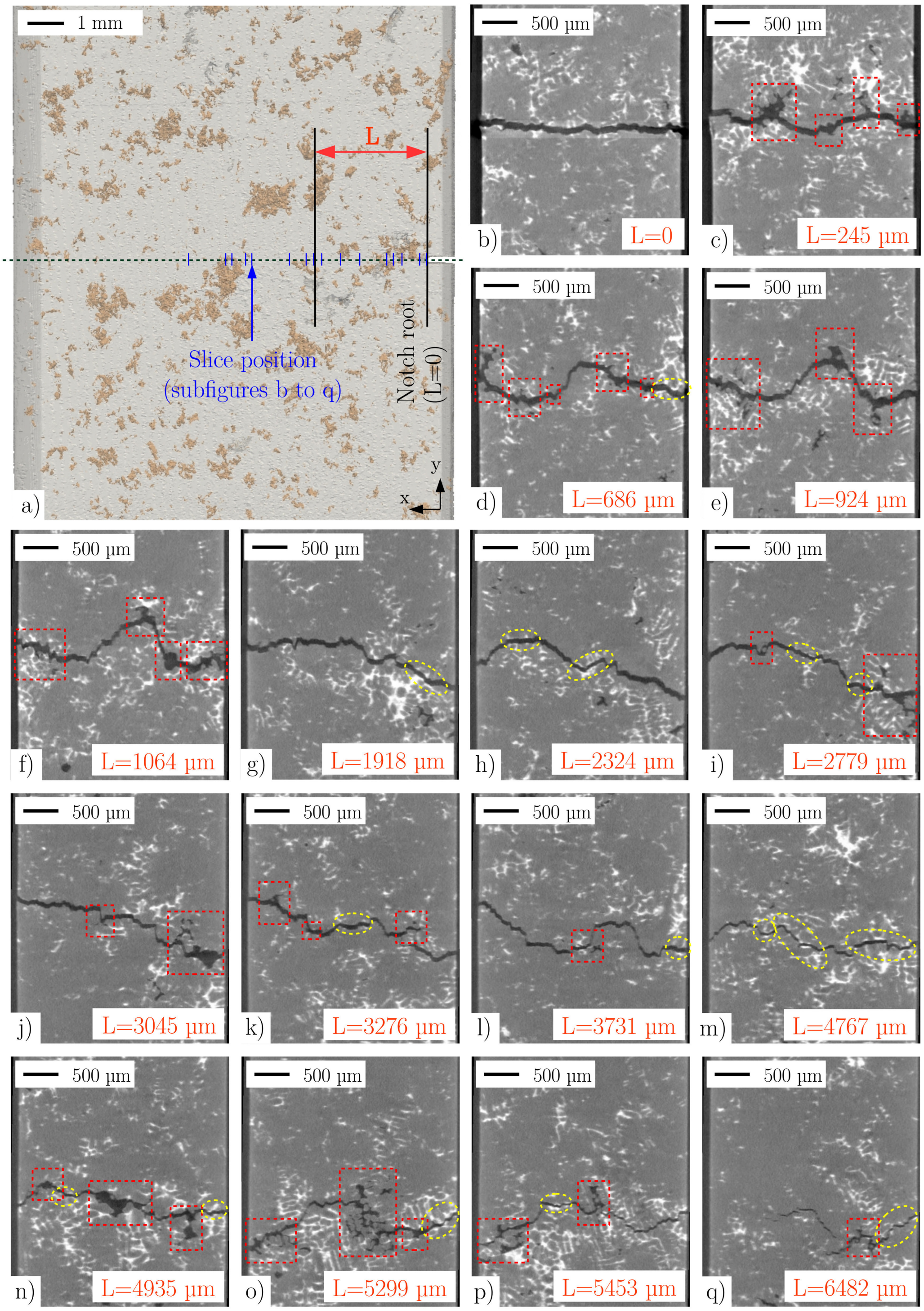

Figure 9: Tomographic analysis of the crack path for specimen P2: (a) 3D rendering of the pores within the gage length, and (b)-(q) tomographic slices parallel to YZ plane located at different distances *L* from the notch root. Crack interaction with pores are highlighted by rectangular boxes (in red) on subfigures (b) to (q) and by ellipses (in yellow) for crack interactions with larges Copper-rich intermetallics.

influence the crack path. A crack acceleration is visible for cracks smaller than 2 mm. Beyond that size, the curve slopes tend to decrease and a FCGR saturation is observed for the longest cracks ($a > 3.5$ mm, except for P1 specimen). Furthermore, for the tested conditions, it appears that there is a steady-state regime independent of local fatigue crack growth accelerations induced by coalescences as visible on figure 5. In the case of the **PF** material, it also appears that FCGR fluctuations are less large that in **P** material (see subfigures 5b and 5c).

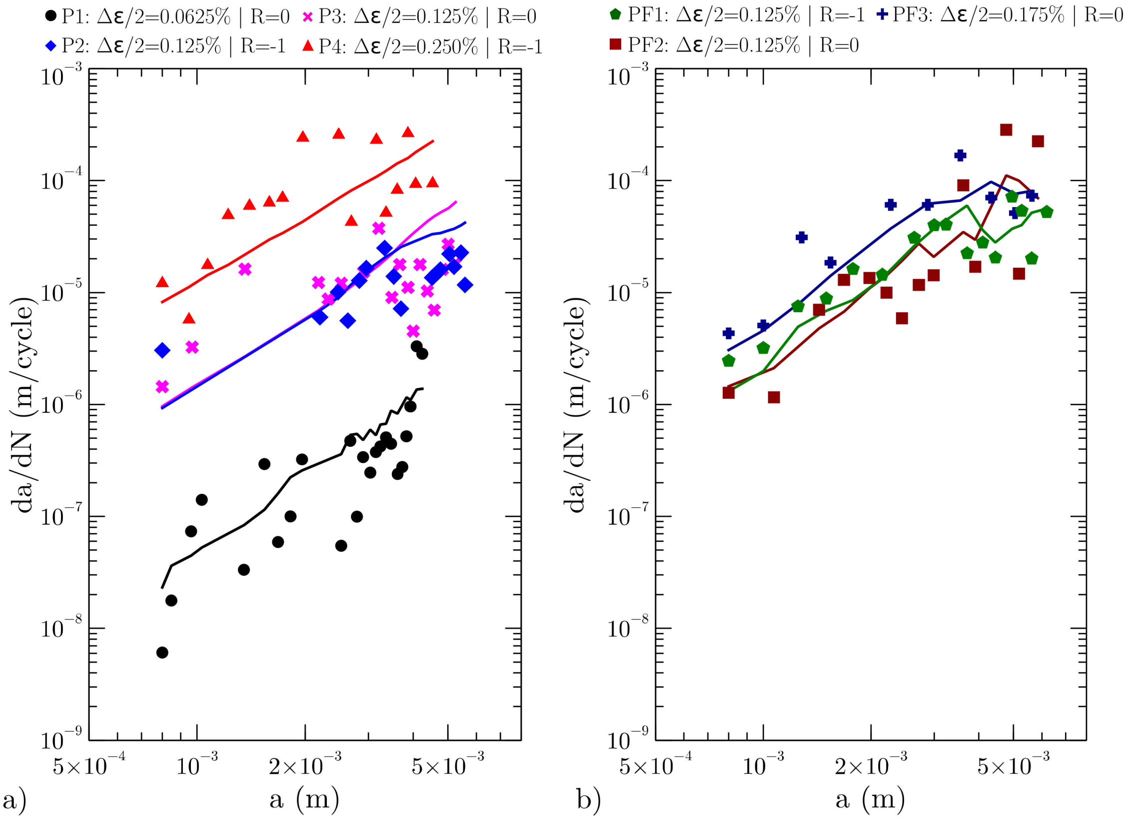

Figure 10: Fatigue crack growth rate as a function of the crack length for (a) porous material and (b) pore-free material. Markers symbolize experimental data, curves correspond to the model [30].

### *4.3. Energetic approach*

As only strain amplitude and hysteresis loops seem to have an influence on FCGR the model of Maurel et al. has been used for FCGR modeling [30, 44]. Numerical results correspond to the curves shown on figure 10. As described on section 3.6 the elastic ($W_e$) and inelastic ($W_p$) energies have to be estimated as inputs to the model. Figure 11 shows the evolution of $W_e$ and $W_p$ as a function of the crack lengths based on equations 3 and 4. Inelastic energies are logically higher than elastic energies for both materials: the ratio $W_p/W_e$ is of the order of 100 in the case of large plastic strains. This ratio is however of the order of 10 for P1 specimen which corresponds to the smallest strain amplitude. The energy levels increase with the strain amplitudes: $W_e$ varies between $10^3$ and $3.5 \cdot 10^4$ J m$^{-3}$ while $W_p$ varies between $3.8 \cdot 10^4$ and $5.0 \cdot 10^5$ J m$^{-3}$. For a specific strain amplitude, $W_p$ however increases to a limit during crack growth although $W_e$ tends to decrease. The model parameters were optimized for both porous and non porous materials and the corresponding values are reported in Table 4. Figure 10 allows to see the good agreement between experimental and numerical results. Despite the chosen macroscopic approach, considering remaining ligament to determine energy evolution is straightforward both to model FCGR decrease observed for long crack and FCGR oscillation observed on PF1 and PF2 specimens.

| Material | m$_e$ | m$_p$ | $\gamma_e$ (J/m$^2$) | $\gamma_p$ (J/m$^2$) |
|---|---|---|---|---|
| LFC | 2.8 | 1.6 | 100 | $1.14 \cdot 10^{+3}$ |
| LFC+HIP+aging | 2.8 | 1.6 | 13.4 | $1.98 \cdot 10^{+3}$ |

Table 4: Model parameters (equation 5) for **P** and **PF** materials. $\lambda$ was fixed to $76.6 \times 10^{-6}$ m.

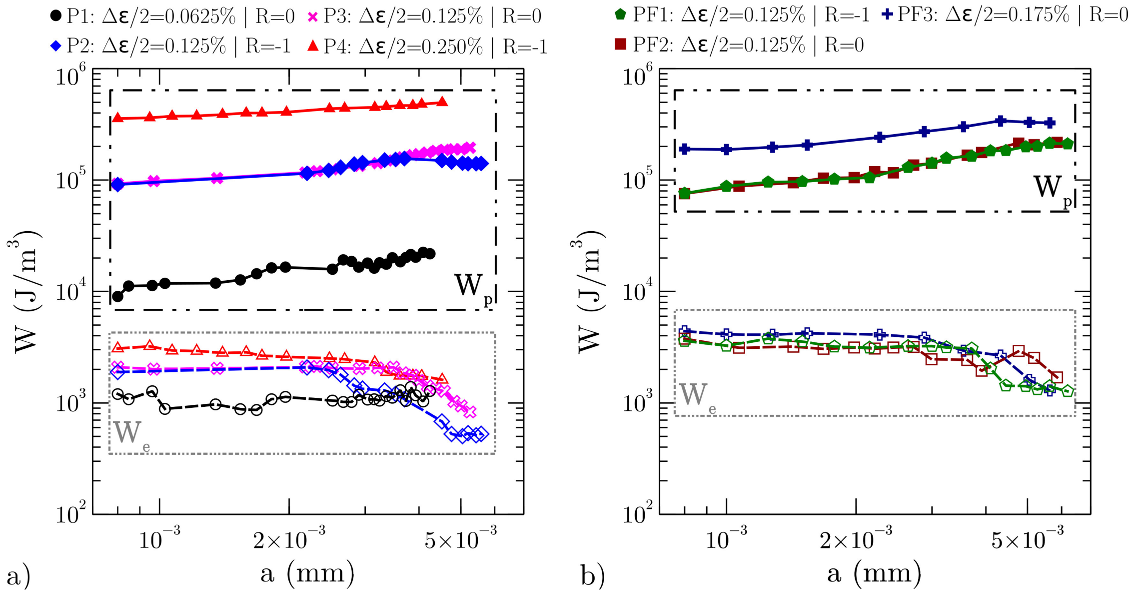

Figure 11: Elastic $W_e$ and inelastic $W_p$ energies as a function of the crack length for the (a) porous and (b) the pore-free material. The effective section reduction of each specimen due to the crack propagation is taken into account for these energies estimations. $W_e$ and $W_p$ evolutions are respectively located inside the bottom box (in light gray) and the upper box (in black).

## 5. Discussion

The high temperature LCF tests performed in this work allow to measure FCGR on material volumes representative of cylinder head inter-valves bridges as the size of those regions is similar to that of the SENT specimens. Large FCGR variations are observed experimentally due to the numerous local crack/microstructure interactions: cracks are "attracted" by pores and eutectic zones (as validated by 3D observations). Secondary cracks are also observed to initiate on pores and hard phases and cause crack accelerations when they coalesce with the main crack. After these accelerations, the main crack returns to its "steady-state" growth rate. As visible on subfigures 5b and 5c the use of a 200 µm crack growth increment to estimate the "steady-state" FCGR is however consistent with the fact that large hard particles sizes drive the crack growth. Nevertheless, crack coalescences and secondary crack initiations are not taken into account here for FCGR modeling. The proposed model was instead based on the assumption of cumulative damage that corresponds to the growth of a single crack [30]. Results are however encouraging.

Crack growth monitoring has shown that crack paths are located within areas that present numerous damaged hard particles. When the material contains pores, crack paths mainly correlate with inelastic strain localizations resulting to the structural effect induced by the largest pores [22]. It is conventionally accepted that strain incompatibilities between the aluminum matrix and hard particles induce particle cleavage/debonding [45, 46]. The mechanical properties (Young modulus and hardness) of the aluminum matrix decrease more than those of other phases at high temperature (Si, AlFeSi intermetallics, Al$_2$Cu) [47]. Strain incompatibilities are therefore more pronounced at high temperatures and increase the probability of initiation of particle damage. However similar crack paths and particle damage are observed for **PF** material. Even if no pore is present, particles are damaged due to the very high level of applied strain:

micro-cracks are associated with broken large particles. The influence of these micro-cracks is comparable to those of pores in the PF material.

Under the studied loading conditions, fatigue crack growth appears to be a successive particle damaging/crack coalescence process. Particles located in front of the crack tip are damaged and the main crack then grows through this damaged zone. The damage localization can be explained by the high levels of inelastic strain in front of the crack tip and by the location of the maximum hydrostatic stress peak just ahead of the crack tip [48]. Particle damage is therefore confined in this area. Similar mechanisms have been observed by Maurel et al. for more microstructurally homogeneous materials during fatigue crack growth testing at high temperature under LCF conditions [44]. Zhao at al. have also observed the same phenomena on stainless steel and have proposed a FCGR model based on a micro-crack density ahead of the crack tip [49]. Finally, the damage mechanisms observed on the SENT test specimens, at the scale of the industrial structure, are similar to those observed *in situ* by X-ray synchrotron tomography on miniature specimens containing only two or three large pores: crack is mainly driven by pores which induced high inelastic strain localizations and are more locally driven by damaged particles [22].

A FCGR model that can be used for part design has been identified. The model proposed by Maurel et al. [30] allows to correctly quantify FCGR for the **P** and **PF** materials. Strain amplitudes and strain ratios are numerically well taken into account using the uni-axial model formulation. Moreover, FCGR variations observed on the curves of figure 10 demonstrate that $W_e$ and $W_p$ are good potential driving forces to model LCF crack growth. These energies are in fact the only quantities used in the model that can explain these variations. The decrease of $W_e$ can be explained by the loss of specimen global stiffness due to the cross section reduction induced by the crack growth. Similarly, the same structure effect is responsible of the $W_p$ increase: plasticity becomes more and more important with the increase of the crack length. Furthermore, $W_e$ and $W_p$ variations are also observed on figure 11 for the longest cracks. Similarities between fatigue crack growth rates and mechanical responses (equivalent to $W_p$ and $W_e$) for specimens subjected to the same strain amplitudes $\Delta\varepsilon/2$ reinforce the interest of an energetic approach even if the influence of porosity on stress values are neglected.

In the case of the pore-free material, $\gamma_e$ and $\gamma_p$ parameters have been re-identified [38] (exponents in equations 5 were kept as constant) because **P** and **PF** materials does not have the same global mechanical behavior (figure 4) while their matrix behaviors (hardness) are similar. This is due to the structural effects induced by large pores that have been previously observed [21, 22]. The global stiffness of a **PF** SENT specimen is higher than that of a **P** SENT specimen. It has been observed in table 4 that the $\gamma_e$ parameter has to decrease while the $\gamma_p$ parameter has to increase in order to better fit experimental curves of figure 10. That means that the elastic energy contribution becomes more important for the **PF** material. In other words, the plastic part plays a major role on crack growth modeling when the material contains pores that induce high strain localizations in their vicinity [22]. Although the crack growth modeling gives good results, model parameters identification was rather difficult due to a coupling between the exponents $m_i$ and the surface energies $\gamma_i$. That is particularly true for the plastic part: $m_p$ gives the curve slopes and also influences the gaps between curves. As a result, and as visible on figure 10a, the best parameters are a trade-off between P1 FCGR slightly overestimation and P4 FCGR underestimation. Deviations between the experimental results and the predicted values can also be explained by the fact that the model does not take into account crack coalescence and secondary crack propagation phenomena.

## 6. Conclusions

Low Cycle Fatigue Crack Growth tests at 250 °C have been performed to study the influence of the microstructure on crack paths and to identify fatigue crack growth rates in the case of specimens submitted to large scale yielding conditions. Two different microstructures of the same cast aluminum alloy have been studied: one containing pores and one without pore obtained by HIP in order to analyze the influence of the casting defects on fatigue crack growth. The main conclusions of this research work are the following:

- Crack paths are globally driven by pores and locally by hard particles for the porous material. In the pore-free material crack paths are only driven by crack/particles interactions.

- Secondary crack initiations located on large hard particles (larger than ≈ 100 µm) and crack coalescence events are observed.
- Larges values of crack growth rates are measured for both materials in the case of large scale yielding: between $10^{-6}$ m/cycle and $10^{-4}$ m/cycle.
- Experimental crack growth rates present a relatively large scatter due to crack/microstructure interactions.
- "Steady-state" fatigue crack growth rates appear to be mostly sensitive to the applied strain amplitude.
- Maurel et al. energetic approach allows to successfully model experimental fatigue crack growth rates. The inelastic and elastic energies proposed by these authors appear to be relevant driving forces for LCF growth rates modeling.

## Acknowledgements

The authors thank the French National Research Agency for funding this study through the ANR project INDIANA (grant ANR-12-RMNP-0011). We also thank the PSA Group and the French National Association for Research and Technology for funding.

## References

[1] European Aluminium Association, Aluminium in cars - unlocking the lightweighting potential, www.european-aluminium.eu/resource-hub (2013).

[2] K. Hoag, B. Dondlinger, Vehicular engine design, Springer, 2016.

[3] M. Javidani, D. Larouche, Application of cast Al-Si alloys in internal combustion engine components, Inter. Mater. Rev. 59 (3) (2014) 132–158. `doi:10.1179/1743280413Y.0000000027`.

[4] H. Arami, R. Khalifehzadeh, M. Akbari, F. Khomamizadeh, Microporosity control and thermal-fatigue resistance of A319 aluminum foundry alloy, Mat. Sci. Eng. A-Struct. 472 (1) (2008) 107–114. `doi:10.1016/j.msea.2007.03.031`.

[5] P. Osmond, étude du vieillissement des alliages d'aluminium pour culasses diesel et prise en compte dans le dimensionnement, Ph.D. thesis, Mines ParisTech (2010).

[6] J. G. Kaufman, E. L. Rooy, Aluminum alloy castings: properties, processes, and applications, ASM International, 2004.

[7] B. Barlas, Etude du comportement et de l'endommagement en fatigue d'alliages d'aluminium de fonderie, Ph.D. thesis, École Nationale Supérieure des Mines de Paris (2004).
URL `https://pastel.archives-ouvertes.fr/tel-00162056`

[8] V.-D. Le, F. Morel, D. Bellett, N. Saintier, P. Osmond, Simulation of the Kitagawa-Takahashi diagram using a probabilistic approach for cast Al-Si alloys under different multiaxial loads, Int. J. Fatigue 93 (2016) 109–121. `doi:10.1016/j.ijfatigue.2016.08.014`.

[9] S. Tabibian, E. Charkaluk, A. Constantinescu, A. Oudin, F. Szmytka, Behavior, damage and fatigue life assessment of lost foam casting aluminum alloys under thermo-mechanical fatigue conditions, Procedia Engineer. 2 (1) (2010) 1145–1154. `doi:10.1016/j.proeng.2010.03.124`.

[10] S. Shivkumar, L. Wang, D. Apelian, The lost-foam casting of aluminum alloy components, JOM-J. Min. Met. Mat. S. 42 (11) (1990) 38–44. `doi:10.1007/BF03220435`.

[11] J. R. Brown, The lost foam casting process, Met. Mater. 8 (10) (1992) 550–555.

[12] Q. Wan, H. Zhao, C. Zou, Effect of Micro-porosities on Fatigue Behavior in Aluminum Die Castings by 3d X-ray Tomography Inspection, ISIJ Int. 54 (3) (2014) 511–515. `doi:10.2355/isijinternational.54.511`.

[13] X. Zhu, J. Yi, J. Jones, J. Allison, A Probabilistic Model of Fatigue Strength Controlled by Porosity Population in a 319-Type Cast Aluminum Alloy: Part I. Model Development, Metall. Mater. Trans. A 38 (5) (2007) 1111–1122. `doi:10.1007/s11661-006-9070-9`.

[14] P. Huter, P. Renhart, S. Oberfrank, M. Schwab, F. Grn, B. Stauder, High-and low-cycle fatigue influence of silicon, copper, strontium and iron on hypo-eutectic AlSiCu and AlSiMg cast alloys used in cylinder heads, Int. J. Fatigue (2016) 588–601.

[15] E. Merhy, L. Rémy, H. Maitournam, L. Augustins, Crack growth characterisation of A356-T7 aluminum alloy under thermo-mechanical fatigue loading, Eng. Frac. Mech. 110 (2013) 99–112. `doi:10.1016/j.engfracmech.2013.03.019`.

[16] D. Tian, X. Liu, G. He, Y. Shen, S. Lv, Q. Wang, Low cycle fatigue behavior of casting A319 alloy under two different aging conditions, Mat. Sci. Eng. A - Struc. 654 (2016) 60–68. `doi:10.1016/j.msea.2015.12.023`.

[17] L. Dietrich, J. Radziejewska, The fatigue damage development in a cast AlSiCu alloy, Materials & Design 32 (1) (2011) 322–329. `doi:10.1016/j.matdes.2010.05.045`.

[18] F. Szmytka, A. Oudin, A reliability analysis method in thermomechanical fatigue design, Int. J. Fatigue 53 (2013) 82–91. `doi:10.1016/j.ijfatigue.2012.01.025`.

[19] J.-J. Thomas, L. Verger, A. Bignonnet, E. Charkaluk, Thermomechanical design in the automotive industry, Fatigue Frac. Eng. M. 27 (10) (2004) 887–895. `doi:10.1111/j.1460-2695.2004.00746.x`.

[20] S. Tabibian, E. Charkaluk, A. Constantinescu, F. Szmytka, A. Oudin, TMF-LCF life assessment of a Lost Foam Casting A319 aluminum alloy, Int. J. Fatigue 53 (2013) 75–81. `doi:10.1016/j.ijfatigue.2012.01.012`.

[21] S. Dezecot, J.-Y. Buffiere, A. Koster, V. Maurel, F. Szmytka, E. Charkaluk, N. Dahdah, A. El Bartali, N. Limodin, J.-F. Witz, In situ 3d characterization of high temperature fatigue damage mechanisms in a cast aluminum alloy using synchrotron X-ray tomography, Scripta Mater. 113 (2016) 254–258. `doi:10.1016/j.scriptamat.2015.11.017`.

[22] S. Dezecot, V. Maurel, J.-Y. Buffiere, F. Szmytka, A. Koster, 3d characterization and modeling of low cycle fatigue damage mechanisms at high temperature in a cast aluminum alloy, Acta Mater. 123 (2016) 24–34. `doi:10.1016/j.actamat.2016.10.028`.

[23] E. Charkaluk, A. Bignonnet, A. Constantinescu, K. Dang Van, Fatigue design of structures under thermomechanical loadings, Fatigue Frac. Eng. M. 25 (12). `doi:10.1046/j.1460-2695.2002.00612.x`.

[24] S. Fontanesi, M. Giacopini, Multiphase CFDCHT optimization of the cooling jacket and FEM analysis of the engine head of a V6 diesel engine, Appl. Therm. Eng. 52 (2) (2013) 293–303. `doi:10.1016/j.applthermaleng.2012.12.005`.

[25] C. Bathias, A. Pineau, Fatigue of materials and structures, John Wiley & Sons, 2013.

[26] B. Tomkins, Fatigue crack propagation and analysis, Philos. Mag. 18 (155) (1968) 1041–1066. `doi:10.1080/14786436808227524`.

[27] R. P. Skelton, Energy criterion for high temperature low cycle fatigue failure, Mater. Sci. Technol. 7 (5) (1991) 427–440. `doi:10.1179/mst.1991.7.5.427`.

[28] C. Shih, J. Hutchinson, Fully plastic solutions and large scale yielding estimates for plane stress crack problems, J. Eng. Mater.-T. ASME 98 (4) (1976) 289–295.

[29] W. Ochensberger, O. Kolednik, Physically appropriate characterization of fatigue crack propagation rate in elasticplastic materials using the j-integral concept, Int. J. Fract. 192 (2015) 25–45. `doi:10.1007/s10704-014-9983-z`.

[30] V. Maurel, L. Rémy, F. Dahmen, N. Haddar, An engineering model for low cycle fatigue life based on a partition of energy and micro-crack growth, Int. J. Fatigue 31 (5) (2009) 952–961. `doi:10.1016/j.ijfatigue.2008.09.004`.

[31] A. Heudt, Etude de la fissuration en plasticité gnralisée de composants moteur du lanceur spatial ariane 5, Ph.D. thesis, Mines ParisTech (2013).

[32] F. Salgado Goncalves, Caractérisation expérimentale et modélisation des interactions entre fissures et perçages multiples à haute température en élastoplasticité généralisée ou confinée, Ph.D. thesis, Mines ParisTech (2013).
URL `https://pastel.archives-ouvertes.fr/tel-01144411`

[33] S. Tabibian, E. Charkaluk, A. Constantinescu, G. Guillemot, F. Szmytka, Influence of process-induced microstructure on hardness of two AlSi alloys, Mat. Sci. Eng. A - Struc. 646 (2015) 190–200. `doi:10.1016/j.msea.2015.08.051`.

[34] Q. G. Wang, D. Apelian, D. A. Lados, Fatigue behavior of A356-T6 aluminum cast alloys. Part I. Effect of casting defects, J. Light Met. 1 (1) (2001) 73–84. `doi:10.1016/S1471-5317(00)00008-0`.

[35] S. Dezecot, M. Brochu, Microstructural characterization and high cycle fatigue behavior of investment cast A357 aluminum alloy, Int. J. Fatigue 77 (2015) 154–159. `doi:10.1016/j.ijfatigue.2015.03.004`.

[36] S. Dezecot, J.-Y. Buffiere, A. Koster, V. Maurel, F. Szmytka, Characterization of damage in a cast aluminum alloy during cyclic loading test at high temperature by x-ray tomography, in: COM 2015-The conference of metallurgists, 2015.
URL `https://hal-mines-paristech.archives-ouvertes.fr/hal-01237859`

[37] H. V. Atkinson, S. Davies, Fundamental aspects of hot isostatic pressing: an overview, Metall. Mater. Trans. A 31 (12) (2000) 2981–3000. `doi:10.1007/s11661-000-0078-2`.

[38] S. Dezecot, Caractérisation et modélisation du rôle des défauts microstructuraux dans la fatigue oligocyclique des alliages d'aluminium de fonderie: application au procédé à modèle perdu., Ph.D. thesis, Institut National des Sciences Appliquées de Lyon (2016).

[39] L. Wang, N. Limodin, A. El Bartali, J.-F. Witz, R. Seghir, J.-Y. Buffiere, E. Charkaluk, Influence of pores on crack initiation in monotonic tensile and cyclic loadings in lost foam casting A319 alloy by using 3d in-situ analysis, Mat. Sci. Eng. A-Struct. 673 (2016) 362–372. `doi:10.1016/j.msea.2016.07.036`.

[40] G. F. Voort, H. James, M. MILLS, J. DAVIS, J. DESTEFANI, D. DIETERICH, G. CRANKOVIC, M. FRISSELL, ASM Handbook: Metallography and Microstructures, ASM International, Materials Park, OH.

[41] R. H. Webb, C. K. Dorey, The Pixilated Image, in: J. B. Pawley (Ed.), Handbook of Biological Confocal Microscopy, Springer US, 1995, pp. 55–67.

[42] Z. Xia, D. Kujawski, F. Ellyin, Effect of mean stress and ratcheting strain on fatigue life of steel, Int. J. Fatigue 18 (5) (1996) 335–341. `doi:10.1016/0142-1123(96)00088-6`.

[43] F. Ellyin, Z. Xia, A general fatigue theory and its application to out-of-phase cyclic loading, J. Eng. Mater.-T. ASME 115 (4) (1993) 411–416. `doi:10.1115/1.2904239`.

[44] V. Maurel, A. Koster, L. Remy, M. Rambaudon, D. Missoum-Benziane, V. Fontanet, F. Salgado-Goncalves, A. Heudt, H. Wang, M. Trabelsi, Fatigue crack growth under large scale yielding condition: the need of a characteristic length scale, Int. J. Fatigue 102 (2017) 184–201. `doi:10.1016/j.ijfatigue.2017.03.021`.

[45] J.-Y. Buffiere, S. Savelli, P.-H. Jouneau, E. Maire, R. Fougeres, Experimental study of porosity and its relation to fatigue mechanisms of model AlSi7Mg0. 3 cast Al alloys, Mat. Sci. Eng. A - Struc. 316 (1) (2001) 115–126. `doi:10.1016/S0921-5093(01)01225-4`.

[46] K. Gall, N. Yang, M. Horstemeyer, D. L. McDowell, J. Fan, The debonding and fracture of Si particles during the fatigue of a cast Al-Si alloy, Mat. Sci. Eng. A - Struc. 30 (12) (1999) 3079–3088. `doi:10.1007/s11661-999-0218-2`.

[47] C.-L. Chen, A. Richter, R. C. Thomson, Investigation of mechanical properties of intermetallic phases in multi-component AlSi alloys using hot-stage nanoindentation, Intermetallics 18 (4) (2010) 499–508. `doi:10.1016/j.intermet.2009.09.013`.

[48] A. Pineau, A. A. Benzerga, T. Pardoen, Failure of metals I: Brittle and ductile fracture, Acta Mater. 107 (2016) 424–483. `doi:10.1016/j.actamat.2015.12.034`.

[49] Y. X. Zhao, Q. Gao, J. N. Wang, Interaction and evolution of short fatigue cracks, Fatigue Fract. Eng. M. 22 (6) (1999) 459–467. `doi:10.1046/j.1460-2695.1999.00195.x`.